LIMNOLOGY
and
OCEANOGRAPHY: METHODS

*Limnol. Oceanogr.: Methods* 12, 2014, 139–154
© 2014, by the American Society of Limnology and Oceanography, Inc.

# A calibration equation for oxygen optodes based on physical properties of the sensing foil

*Craig L. McNeil* and Eric A. D'Asaro*
Applied Physics Laboratory and School of Oceanography, University of Washington

## *Abstract*

We present a new physically based calibration equation for Aanderaa Inc. oxygen sensing optodes. We use the two site fluorescence quenching model of Demas et al. (1995) to describe the nonlinear Stern-Volmer response of the optode foil to oxygen partial pressure. Seven (minimally six) coefficients quantify foil response to oxygen and temperature; another quantifies response to hydrostatic pressure. These eight coefficients are related, theoretically, to basic physical properties of the foil. The equation provides a framework to study causes of variability and drift in optodes and to develop better quality control and handling procedures. We tested the equation using factory calibrations of 24 optode foils. When accurate multi-point calibration data are unavailable, two additional coefficients empirically correct the usually large differences observed between factory foil calibrations and post-factory laboratory/field calibrations; we cannot eliminate this major cause of uncertainty in optode calibrations. Excluding two potentially anomalous foils, the calibration equation fits 13 similarly calibrated foils, totaling 455 calibration points over 3 – 40°C to –0.57 ± 1.48 mbar. Analysis of the resulting best fit coefficients reveals an underlying variability in optodes associated with variability in site 2 and site 1 Stern-Volmer coefficients of 32% and 20%, respectively. The fraction of unquenched fluorophores responding with the more accessible site 1 quenching characteristics varies by only 3%. The equation fits multi-point data for two optodes within manufacturer's specifications, the greater of ± 2.5 μmol kg$^{-1}$ and ± 1.5%. Detailed measurements of calibration changes over time will be required to understand the causes of optode drift.

Dissolved oxygen is the next most widely measured property of seawater after temperature and salinity (Boyer et al. 2009). Dissolved oxygen (DO) sensors are standard additions on oceanographic CTDs and underway systems. DO measurements provide an additional parameter with which to identify water masses, and one can easily infer the biological history of those waters from apparent oxygen utilization (AOU) estimates. DO sensors are also frequently used on autonomous platforms (e.g., moorings, floats, gliders, profilers, AUVs, benthic landers) to study a variety of processes and environments. Some examples of studies that use DO sensors include net ecosystem metabolism (Emerson and Stump 2010; Fiedler et al. 2012; Martz et al. 2008; Riser and Johnson 2008), air-sea gas exchange (D'Asaro and McNeil 2007; Körtzinger et al. 2004), oxygen minimum zones (Revsbech et al. 2009), phytoplankton blooms (Perry et al. 2008), benthic respiration rates (Frederiksen and Glud 2006; Wikner et al. 2013), and lake/reservoir benthic $O_2$ flux (McGinnis et al. 2008).

With extensive use of DO sensors in fresh and saltwater, there is great demand for DO sensors with improved specifications. Particular attention is given to long-term calibration drift when used in remote oceanographic applications because seasonal changes in surface $O_2$ over most of the world oceans are small, only 25–40 μmol$O_2$ kg$^{-1}$ per year at time series stations BATS and OWS-P (McKinley et al. 2000; Steiner et al. 2007). Inter-annual decrease in upper ocean oxygen content, which is thought to be associated with global warming impacts (Gruber 2011), is even smaller: on average –0.66 μmol kg$^{-1}$ per decade at 300 dbar (Stramma et al. 2012).

An additional complication is that DO sensors are subjected to different usage histories depending on the platform used. For example, an optode on an Argo float spends most of its time in the cold dark deep ocean (see Riser and Johnson

*Corresponding author: E-mail: cmcneil@apl.washington.edu; 1013 NE 40th St., Seattle, WA USA 98105; Tel: 206-543-2157

***Acknowledgments***

We are grateful to Roberta Hamme (Univ. of Victoria, B.C., Canada) who pointed out to us the pressure dependence of Henry's Law $O_2$ solubility coefficients and provided us with relevant references. We thank two anonymous reviewers for greatly improving the manuscript and providing, along with Aanderaa Inc. representative Shawn Sneddon, additional calibration data sheets for use in this study. CLM was supported by the NSF (OCE-0834340, OCE-1153295, OCE-0424602) and NOAA (NA09-OAR-4310061). EAD was supported by NSF (OCE-0549887).

DOI 10.4319/lom.2014.12.139

2008: Online Methods section) in contrast to one on a long-term surface mooring constantly exposed to warmer waters and sunlight (Bushinsky and Emerson 2013). An optode on an AUV, however, likely spends less than 10% of the time in the water over its lifetime and is stored in a warm laboratory. Platform-dependent customization usually occurs. For example, AUV's require short sensor response time and one commonly uses a foil that does not have an opaque outer coating. The disadvantage of such 'fast' foils is that they are much more susceptible to photo-bleaching effects from sunlight when in use and need to be stored with light protection caps on. The challenge of developing improved procedures to mitigate such calibration drift is hampered by the lack of understanding of the causes of sensor drift.

Motivated by the need to better understand optode calibration drift, we derive a new calibration equation focused on the physicochemical properties of the optode foil. We model the foil response using a non-linear, rather than linear, Stern-Volmer equation. This allows us to capture more subtle information on the foil properties when fitting to calibration data. The resulting calibration equation has eight (minimally seven) coefficients each with a clear physical interpretation. This takes the first step towards improved quality control of optodes, and hence optode data, based on the physical characteristics of the sensor's foil. For example, by applying this method to 24 factory calibration sheets, we will show that one foil responds using an anomalously high fraction of fluorophores located in sites poorly accessible to oxygen. Another foil operating in warm water shows a negative Arrhenius activation energy for fluorophore self-quenching in the absence of oxygen. Future work is needed to apply the new calibration equation to improve understanding of known calibration drift of sensors (e.g., D'Asaro and McNeil 2013; Tengberg and Hovdenes 2013). This next step is expected to provide a better understanding of calibration drift with use on different oceanographic platforms, and ultimately improved practices for sensor handling and storage.

**Background**

There are three standard approaches to measuring dissolved oxygen in natural waters. The first is the century old Winkler titration technique that involves chemical analysis of seawater samples taken from depth (e.g., Culberson and Huang 1987). It is the primary standard for accurate measurement of dissolved $O_2$ but requires significant investment in laboratory equipment and personnel training. It is, and will likely remain for the foreseeable future, a requirement for precise in situ calibration of DO sensors.

Two real time output DO sensor technologies have been refined over the years: the electro-chemical oxygen sensor (polarographic) and the optical sensor (optode). Both sensors come in various shapes and sizes with a large range of $O_2$ (and thermal) response times, sensitivities, and potential for interferences, calibration drift, freezing impacts, etc. Sensors range from micro-electrodes and optical fibers (e.g., Hasumoto et al. 2006; Kilimant et al. 1995), to large planar sheet optodes for use in sediment studies (Larsen et al. 2011), to the more standard sensors attached to rosette CTDs and other autonomous platforms. The Sea-Bird Electronics Inc. SBE-43 polarographic $O_2$ sensor is perhaps the most commonly used sensor on profiling CTDs due its relatively fast response, although the company also now offers their own version of an oxygen optode. Comparisons of SBE-43 and Aanderaa optode against Winkler titration measurements are reported elsewhere (e.g., Körtzinger et al. 2005; Bushinsky and Emerson 2013; D'Asaro and McNeil 2013). Although the commercial Aanderaa Inc. optode is the focus of this study, there are also other similar designs reported in the literature (Kostov et al. 2000). Optode technologies take advantage of a phenomenon called dynamic fluorescence quenching; in the presence of oxygen, certain fluorescent compounds exhibit reduced emission intensity and increased emission delay.

The commercial Aanderaa optode was described by Tengberg et al. (2006). The Aanderaa optode has an external sensing foil in direct contact with seawater. The foil is composed of an indicator layer which sits on top of a thin polyester (we assume Mylar) substrate. The indicator layer is a fluorescent platinum porphyrin complex embedded in a polymer layer (we assume silicone based, such as PDMS). The foil is illuminated through a window in the sensor housing by a blue/green excitation light emitting diode (LED), modulated at 5 kHz. The red fluoresced light given off by the foil is received by a photodiode detector. Optical filters reduce reflected light from entering the photodiode directly from the emitter. Although the detector measures the intensity of the fluoresced light, the intensity is sensitive to the optical coupling and any photo-bleaching of the foil with use. Lifetime of the excited fluorophores in the foil relative to the excitation light is a much better measurement of oxygen quenching than intensity. Lifetime is measured, indirectly, by the phase delay between the excitation and emission (Bailey and Rollefson 1953). An additional red LED is included as a non-excitation reference as a means to compensate for potential drift in the electronics of the transmitter and receiver circuit. This feature was not used in the interpretation of the data in earlier models, but is in newer models (e.g., model 4330).

The standard Aanderaa calibration procedure uses a 22 coefficient polynomial regression fit to laboratory data collected over a range of temperature and dissolved oxygen concentration. Uchida et al. (2008) made a significant contribution to calibration approaches for the Aanderaa Inc. optode by reducing the number of empirically derived calibration coefficients recommended in the manual from 22 to 7 (although our review of their method suggests that 8 coefficients would be more appropriate). One additional coefficient associated with corrections for hydrostatic pressure was determined more precisely, for a total of 8 coefficients. Uchida et al. (2010) subsequently showed how to reduce the number of coefficients by one by combining coefficients.

## Materials and procedures

**Linear Stern-Volmer relationship**

Oxygen is the dynamic quenching agent in the foil of the optode. It decreases the intensity of the foil's fluorescence emission and decreases the lifetime of the excited state of the luminophores. The linear Stern-Volmer equation relates lifetime to oxygen and is derived using bimolecular quenching kinetics to be:

$$\frac{\tau_o}{\tau} = 1 + K_{SV} \cdot p_{O2} \tag{1}$$

where $p_{O2}$ [mbar] is the partial pressure of oxygen, $\tau_o(T)$ [s] is the lifetime under anoxic conditions at temperature, $T$ [°C], and $\tau(p_{O2}, T)$ [s] is the lifetime under operating conditions. The Stern-Volmer constant, $K_{SV}$ $(T)$ [mbar$^{-1}$], which indicates the sensitivity of the luminophores to oxygen, can be further separated as

$$K_{SV}(T) = k_Q(T) \times \alpha(T) \times \tau_o(T) \tag{2}$$

where $k_Q$ [mol$^{-1}$ L s$^{-1}$] is the bimolecular quenching constant, and $\alpha$ [mol L$^{-1}$ mbar$^{-1}$] is the Henry's Law oxygen solubility coefficient for the foil (Demas et al. 1995). Fundamentally, $k_Q$ reflects the efficiency of quenching or accessibility of the luminophores to oxygen and can be written as:

$$k_Q = f_Q \times k_D \tag{3}$$

where $f_Q$ [dimensionless] is the quenching efficiency, or the mean fraction of collisions between excited fluorophores and oxygen molecules that do not result in fluorescent emissions, and $k_D$ [mol$^{-1}$ L s$^{-1}$] is the diffusion-controlled bimolecular rate constant. The Smoluchowsi equation can be used to describe the probability of collisions between an excited fluorophore and a quenching oxygen molecule as:

$$k_D = 4\pi c_1 N r D \tag{4}$$

where $c_1 = 10^3$ [L m$^{-3}$] is a volumetric conversion factor, $N$ [mol$^{-1}$] is Avogadro's number, $r$ [m] the effective collisional radius of the interacting molecules, and $D$ [m$^2$ s$^{-1}$] the effective diffusivity where effective properties are assumed to be the sum of the individual properties for both the fluorophore and oxygen molecules (Lakowicz 1999). Since the fluorophore is bound within the foil, the effective diffusivity is simply the molecular diffusivity of oxygen in the foil's polymer layer which could equally be expressed in terms of the foil's permeability, $P_f$, to oxygen as $P_f = \alpha \times D$ [kmol m m$^{-2}$ s$^{-1}$ mbar$^{-1}$; the second and third terms refer to the foil's thickness and cross-sectional area, respectively].

**Phase delay measurement**

Lifetime is a function of the phase shift of the received red luminesced light (Tengberg et al. 2006). The following relationship converts between phase and lifetime:

$$\frac{\tau_o}{\tau} = \frac{\tan(\varphi_o)}{\tan(\varphi)} \tag{5}$$

where $\varphi$ [deg] is the measured phase delay under operating conditions, and $\varphi_o$ [deg] denotes anoxic conditions (Demas et al. 1999). Lifetime is then calculated using Eq. 5 to be $\tau_o = \tan(\varphi_0)/(2\pi f_m)$ where $f_m$ = 5 kHz the modulation frequency of the foil.

**Factory calibration of the foil**

Optode foils are batch calibrated for Aanderaa Inc. by the vendor at 35 setpoints in freshwater, at 5 temperatures over the range of approximately 3°C – 40°C and 7 oxygen levels over the range 0–300 mbar. Oxygen partial pressure in the headspace of the water bath is in equilibrium with the water at each setpoint. Corrections for vapor pressure of water are necessary since the calibrations are performed at different temperatures and the vapor pressure of water is a function of temperature (Kennish 1989). Uchida et al. (2008) and others chose to work with the calibration data expressed in term of oxygen concentration of the water. We choose to work with oxygen partial pressures since the optode fundamentally measures oxygen partial pressure in the foil, rather than concentration (Demas et al. 1999). We use Henry's Law and solubility coefficients of García and Gordon (1992), their Table 1, Column 3 and corrected Eq. 8, with appropriate water vapor corrections, to convert between concentrations and partial pressures.

It is well known that the factory calibrations of Aanderaa optodes, although presumably accurate at the time of measurement, underestimate true oxygen concentration by approximately 10% for a newly delivered optode. This introduces a major uncertainty into the sensor calibration for end users since the cause of this problem, and thus its solution, is unknown. Perhaps the foil characteristics change during the time period between foil calibration and installation of the foil on a new optode; perhaps this calibrates the differences between the individual optode's measurement of phase and that used in the factory. Since here we work only with the factory calibration data, we emphasize at the outset that application of our new method to the standard factory calibration data will not remove this offset. Although we are uncertain of its accuracy and meaning, we must also include the same empirical correction to this problem that the manufacturer recommends by applying additional two-point calibration after the optode is calibrated to the foil calibration data. Statistical analysis of foil calibration data that spans a large range of foil storage history may reveal why this persistent delivery problem occurs, but this is not attempted here. This additional corrective step is, of course, unnecessary if users apply our calibration equation to their own sufficiently complete post-delivery calibration data set or an advanced multi-point factory calibration data set.

**Non-linear Stern-Volmer relationship**

A linear Stern-Volmer equation is best suited to describing a liquid medium, whereas in a solid medium, such as polymer films, a downward curvature on the Stern-Volmer plot is common (see Theoretical section of Li and Wong 1992 and references 8–10 therein). This downward curvature, or non-linear response, can be described using a non-linear Stern-Volmer equation. Best fit coefficients of the nonlinear equation are more likely to capture subtle information on the foil response than best fit coefficients of the linear model. Moreover, the possibility of identifying the cause of foil aging effects increases if changes in the nonlinear Stern-Volmer coefficients over time can be attributed to physical causes. We, therefore, chose to calibrate the optode by fitting to a nonlinear Stern-Volmer equation.

Two models have been proposed to describe the common finding that Stern-Volmer deviates from a linear relationship. The first model conceptualizes the embedded luminophores as occupying two, or more, sites within the foil. Each site is considered to have its own characteristic quenching constants (Carraway et al. 1991; Sacksteder et al. 1993). For an optode, if some fluorophores in the foil are accessible to oxygen by diffusion while others are not, fluorophores at both sites still fluoresce when stimulated with blue light, but only those sites accessible to oxygen contribute to a reduction in the intensity of the fluoresced red light. The second model conceptualizes that micro-voids within the polymer matrix of the foil, and associated Langmuir adsorption of oxygen in these micro-voids, imparts the foil with nonlinear oxygen solubility dependence (Li and Wong 1992). Thus, fluorophores with higher oxygen content in the vicinity of micro-voids will be subjected to greater dynamic quenching. This creates an analogous situation to the two-site model since both sites have different quenching constants, but the conceptual models differ in the mechanism for why different sites may exist. Demas et al. (1995) reviewed both models, concluding that both are mathematically identical when used as a means to calibrate an optode, but stated preference for the first model since, they argued, the derived coefficients were more meaningful in terms of understanding the foil's luminescence response. Therefore, we also chose to use this first model and assume two sites as a basis for calibrating an Aanderaa optode. The two site nonlinear Stern-Volmer equation is given by

$$\frac{\tau_o}{\tau} = 1 / \left\{ \left[ \frac{f_{o1}}{1 + K_{SV1} p_{O2}} \right] + \left[ \frac{1 - f_{o1}}{1 + K_{SV2} p_{O2}} \right] \right\} \quad (6)$$

where the subscripts '1' and '2' denote the two types of sites and $f_{01}$ [dimensionless] is the fractional contribution to the unquenched steady-state emission at the monitoring wavelength at type 1 sites (Demas et al. 1995). Type 1 sites are considered as the majority and easily accessible sites, and type 2 sites as the minority and poorly accessible sites. The total number of model coefficients that describe the foil's fluorescence characteristic is six (i.e., $K_{SV1} = k_{Q1} \times \alpha_1 \times \tau_{o1}$ and $K_{SV2} = k_{Q2} \times \alpha_2 \times \tau_{o2}$), but we really only need to fit the calibration data to two coefficients (i.e., $K_{SV1}$ and $K_{SV2}$) to capture the essence of this model.

Eq. 6 is an invertible function and therefore has a root that facilitates incorporation of the coefficients derived from the nonlinear Stern-Volmer fits directly into an analytical calibration equation given as:

$$\begin{aligned} p_{O2} = & \left[ (\tau_o / \tau)\left(K_{SV1} - f_{o1}K_{SV1} + f_{o1}K_{SV2}\right) - \left(K_{SV1} + K_{SV2}\right) \right. \\ & + sqrt\left\{ (\tau_o / \tau)^2 \left( -2 f_{o1} K_{SV1}{}^2 + f_{o1}{}^2 K_{SV1}{}^2 + f_{o1}{}^2 K_{SV2}{}^2 \right. \right. \\ & + 2 f_{o1} K_{SV1} K_{SV2} - 2 f_{o1}{}^2 K_{SV1} K_{SV2} + K_{SV1}{}^2 \left. \right) + 2(\tau_o / \tau)\left( f_{o1} K_{SV1}{}^2 \right. \\ & \left. - f_{o1} K_{SV2}{}^2 - K_{SV1}{}^2 + K_{SV1} K_{SV2} \right) + \left( K_{SV1}{}^2 + K_{SV2}{}^2 \right. \\ & \left. \left. - 2 K_{SV1} K_{SV2} \right) \right\} \left. \right] / \left[ 2 K_{SV1} K_{SV2} \right] \end{aligned} \quad (7)$$

Substituting Eq. 5 into Eq. 7 expresses the calibration equation in terms of the raw optode phase measurement at fixed temperature. This is a general solution calibration equation and can be used as is with no further simplifications.

**Temperature compensation**

The foil's response to oxygen is sensitive to temperature. We expect this since molecular diffusivity increases with temperature and so the collisional frequency of the oxygen molecules with the luminophores will also increase with temperature. Since $\tau_o$ normalizes the Stern-Volmer equation, it provides partial temperature compensation from a calibration point of view so choosing an appropriate functionality with temperature is important.

We chose to fit $1/\tau_o(T)$ using an Arrhenius equation since we are dealing with a temperature dependent rate problem, hence

$$\frac{1}{\tau_0(T)} = \frac{1}{\tau_0'} . e^{-E_{\tau 0} / \left( R \left( T + 273.15 \right) \right)} \quad (8)$$

where the pre-exponential term $\tau_o'$ [s] is a constant independent of temperature, $E_{\tau o}$ [J mol$^{-1}$] is an activation energy, $R$ = 8.3144621 [J K$^{-1}$ mol$^{-1}$] the Gas Constant, and $T$ [°C] is temperature. Higher temperatures shorten the lifetime, implying that the probability of thermal quenching of a fluorophore is increased. We interpret $E_{\tau o}$ to be the minimum kinetic energy that a significant fraction of the foil's embedded fluorophores must have for thermal quenching effects to significantly alter the foil's response in the absence of oxygen. Therefore, $E_{\tau o}$ expresses the bulk sensitivity of the embedded fluorophores' self-quenching rate to temperature. After best fitting the zero $O_2$ calibration data to an Arrhenius curve, we use that curve to calculate interpolated values of $\tau_o$ at $T = T_c$, where $T_c$ [°C] is the calibration setpoint temperatures. Then, having values of $\tau_o(T = T_c)$, we use Eq. 5 to calculate values of $\tau_o/\tau$ for each setpoint. The collection of calibration foil data at any particular $T_c$ we will call an 'isothermal response curve'. Note that this procedure only partially compensates the optode's response to temperature.

The foil's dynamic quenching response to oxygen is also temperature sensitive. When an $O_2$ molecule strikes an excited fluorophore, it deactivates it, preventing release of the photon, so warming up the membrane allows the $O_2$ molecules in the membrane matrix to diffuse faster, and therefore, have a higher probability of hitting the next excited fluorophore and deactivating it. The next step is to collapse the isothermal response curves, as discussed above, onto one normalized temperature response that best spans the sensor's operating range of interest for data collection. To do that, we need to determine the temperature dependence of the foil coefficients in response to oxygen, namely $K_{SV1}$, $K_{SV2}$, and $f_{01.}$

To reduce the number of calibration coefficients, we will assume that $\beta = K_{SV1}/K_{SV2}$ [dimensionless] is constant and therefore independent of temperature. This assumption imparts the same (percentage) temperature dependency of $K_{SV1}$ to $K_{SV2}$. This is justified based on the fact that $K_{SV2}$ is subject to the same controlling thermodynamics, and it is a second-order term with less impact on the calibration curves than $K_{SV1}$. As we shall see, the factory calibration data indicate that $f_{01}$ is nearly constant and that $K_{SV1}$ is most sensitive to temperature, as we might expect. We can rewrite Eq. 7 as

$$pO_2 = \frac{\beta}{2K_{SV1}} \times \left[ (\tau_o/\tau)\left(1 + \frac{f_{o1}}{\beta} - f_{o1}\right) - \left(1 + \frac{1}{\beta}\right) + sqrt\left\{(\tau_o/\tau)^2\left(-2f_{o1} + {f_{o1}}^2 + \frac{{f_{o1}}^2}{\beta^2} + \frac{2f_{o1}}{\beta} - \frac{2{f_{o1}}^2}{\beta} + 1\right) + 2(\tau_o/\tau)(f_{o1} - f_{o1}/\beta^2 - 1 + 1/\beta) + (1 + 1/\beta^2 - 2/\beta)\right\}\right] \quad (9)$$

The simplest model of the temperature dependence of $K_{SV1} = f_{Q1} \times k_{D1} \times \alpha_1 \times \tau_{o1}$ is to assume that the bimolecular quenching rate, $k_{D1}$, is fully controlled by the diffusion rate of oxygen in the foil, and therefore, the Stokes-Einstein equation:

$$k_{D1}(T) = \frac{2R(T + 273.15)}{3\eta} \quad (10)$$

where $\eta$ [kg $s^{-1}$ $m^{-1}$] is the effective viscosity of the gas in the polymer foil. However, given that we have already chosen to specify $\tau_{o1}$ by an Arrhenius equation, and $\alpha_1$ has some unknown temperature dependence but likely governed by Van't Hoff type equation, we also chose to fit $K_{SV1}$ to an Arrhenius equation:

$$K_{SV1}(T) = K'_{SV1}.e^{-\frac{E_{SV1}}{R(T+273.15)}} \quad (11)$$

where the pre-exponential term $K_{SV1}'$ [$mbar^{-1}$] is a constant independent of temperature and $E_{SV1}$ [J $mol^{-1}$] an activation energy.

If $\beta$ is strongly temperature dependent, and the assumption of a constant value introduces unacceptable error, then one also needs to fit $K_{SV2}(T)$ using the same form as Eq. 11 and retain this temperature dependence in the equations. Note that the exponent of $\beta$ would then depend on the difference in the activation energies, $E_{SV1} - E_{SV2}$.

To summarize, the main temperature dependence of the foil comes from $K_{SV1}(T)$, with some additional dependence from $\tau_o(T)$, which was imposed using Eq. 8 before fitting the calibration data to the two site Stern-Volmer model. The final step in temperature compensation is to collapse all isothermal calibration curves onto one isothermal calibration curve at a standard temperature, $T_s$. This standardized calibration curve can then be used as a convenient 'lookup table' for calibrated oxygen at other temperatures and phase shift. This approach also makes it easy to compare the response of different optodes to oxygen, independent of temperature response, when different optodes are calibrated at different temperature setpoints (e.g., multi-point calibrations). For our assessment, we will normalize the optode's response curves to the mid-range of the factory supplied calibration data, but this temperature should be chosen to suit the intended use of the sensor in the field. For example, if the sensor is to be used in the Arctic, then one might choose $T_s$ = 5°C. By using Eq. 9 to describe laboratory calibration data measured at a standardized temperature, $p_{O2}(T_s)$, calibrated oxygen at other temperatures and phase shift can be determined using

$$p_{O2}(T) = p_{O2}(T_s) \times \frac{\gamma(T)}{\gamma(T_s)} \times \frac{K_{SV1}(T_s)}{K_{SV1}(T)} \times \frac{\beta(T)}{\beta(T_s)} \quad (12a)$$

where:

$$\gamma(T) = \left[(\tau_o/\tau)\left(1 + f_{o1}/\beta - f_{o1}\right) - \left(1 + 1/\beta\right) + sqrt\left\{(\tau_o/\tau)^2\left(-2f_{o1} + {f_{o1}}^2 + {f_{o1}}^2/\beta^2 + 2f_{o1}/\beta - 2{f_{o1}}^2/\beta + 1\right) + 2(\tau_o/\tau)\left(f_{o1} - f_{o1}/\beta^2 - 1 + 1/\beta\right) + \left(1 + 1/\beta^2 - 2/\beta\right)\right\}\right] \quad (12b)$$

where $\tau_o(T)$ is given by Eq. 8, $K_{SV1}(T)$ and $\beta = K_{SV1}(T)/K_{SV2}(T)$ by Eq. 11, and $\tau = \tan(\varphi)/(2\pi f_m)$ from Eq. 5. Note that we have left the possibility of a temperature dependent $\beta(T)$ in Eq. 12a; if it is constant and independent of temperature then the last term becomes unity. We now have a fully temperature-compensated calibration equation that best matches the manufacturer's foil calibration data according to the imposed functional dependencies of the two site Stern-Volmer model.

**Pressure compensation**

Pressure compensation of the optode is required when using it deep in the ocean. Uchida et al. (2008) refined the magnitude of the pressure correction term proposed in the manual (i.e.., 4.0% per 1000 dbar) to 3.2% per 1000 dbar. The source of this pressure compensation is not discussed in the manual nor in any prior publications on the optode (e.g., Tengberg et al. 2006; Uchida et al. 2008). We now discuss this in more detail.

The fact that pressure compensation of the optode is even required strongly suggests that it is related, somehow, to pressure dependence of an oxygen solubility coefficient. The two

primary solubility terms are that of seawater ($\alpha_{sw}$) and the foil ($\alpha_1$). Note that we are defining solubility coefficients that are the inverse of the classical Henry's Law solubility coefficients (i.e.., we are using $[O_2] = \alpha \times pO_2$ rather than $[O_2] = pO_2/K_H$). It has recently come to our attention (courtesy of Roberta Hamme, UVic) that the fugacity of oxygen, $fO_2$ [mbar], in an equilibrated water sample, with constant oxygen concentration, increases under increased hydrostatic pressure of the water, $P_w$ [dbar]. In other words, the gas solubility $\alpha$ decreases with increasing hydrostatic pressure. There are a series of older papers that addressed this issue motivated, in part, by the need to understand fish swim bladder maintenance in the deep ocean (Klots 1961; Enns et al. 1965). Some confusion arose in the literature over one study in particular (Carey and Gibson 1976) that used fluorescence quenching to try to sense this fugacity change. The fluorescent dye solution used in the experiment did not show any significant decrease in fluorescence emission intensity under increased pressure. A subsequent study (Taylor 1978) suggested that a compensating decrease in the bimolecular quenching constant may occur commensurate with an increase in the partial pressure of oxygen under pressure, and proposed a theoretical relationship for the increase in oxygen partial pressure with increasing hydrostatic pressure as

$$fO_2 = pO_2 \exp\left(\frac{Vo_2 P_w}{\Theta c_2 R\left(T+273.15\right)}\right) \quad (13)$$

where $fO_2$ [mbar] is the in situ fugacity of oxygen at depth, $pO_2$ [mbar] is the partial pressure of oxygen referenced to the sea surface, and $Vo_2$ [mL $O_2$ mol$^{-1}$] is the partial molar volume of oxygen in solution, $R$ = 82.05 [mL$O_2$ atm mol$^{-1}$ K$^{-1}$, units appropriate here], and potential temperature $T$ [°C], and $c_2$ = 10.1325 [dbar atm$^{-1}$] is a pressure conversion factor. We include in Eq. 13 an empirically determined scale factor, $\Theta$ [dimensionless]. Subsequent work confirmed the dependence of gas solubility with pressure (e.g., Kennan and Pollack 1990). From Enns et al. (1965), $Vo_2$ = 31.7 ± 0.2 [mL $O_2$ mol$^{-1}$] in seawater. For example, if $\Theta$ = 1, $T$ = 5°C and $pO_2(P=0)$ = 200 mbar, then $fO_2(P=1000)$ = 229 mbar, representing an increase of approximately 14% per 1000 dbar. This dependence is much larger, and of opposite sign, to that observed by Uchida et al. (2008), who found that the optode readings decreased by 3.2% per 1000 dbar.

Seeing no obvious alternative explanation, we likewise follow Taylor's (1978) lead and assume that the bimolecular quenching constant ($k_Q$) of the optode's foil is reduced under pressure. Thus, we assume that the foil is desensitized by approximately 17.2% per 1000 dbar response due to an intrinsic decrease in the quenching efficiency ($f_Q$) and/or diffusion-controlled bimolecular rate constant ($k_D$). This interpretation seems preferable to the alternative interpretation that the foil's solubility to oxygen ($\alpha_1$) is decreased because there was no foil involved in Carey and Gibson's (1976) work, which used a liquid fluorescent dye.

To estimate the scale factor $\Theta$, we use the Uchida et al. (2008) finding that the optode response decreases by 3.2% per 1000 dbar and calibrate to a deep ocean temperature, $T_d$ [°C], and hydrostatic pressure, $P_d$ [dbar]. Multiplying the righthand side of Eq. 13 with variable $\Theta$ by a factor of $(1 - 3.2\times10^{-5}\times P_d)$, and equating to the true in situ partial pressure that is obtained using Eq. 13 with $\Theta$ = *1*, we can solve for the scale factor:

$$\Theta = 1/\left[1-\ln\left(1-3.2\times10^{-5}P_d\right)\left(c_2 R T_d\right)/\left(V_{O2}P_d\right)\right] \quad 14$$

We calibrate to Uchida's deep ocean values using $T_d$ = 1°C and $P_d$ = 6000 dbar, hence from Eq. 14 we calculate $\Theta$ = 0.7965. Using $\Theta$ = 0.7965 therefore calibrates Eq. 13 to field data.

**Two-point calibration**

Although we do not understand why a standard delivered optode differs from the factory calibration, we use the same approach suggested in the Aanderaa manual, adjusting the measured phase to two-point measurements at $pO_2$ = 0 and 100% (using sodium sulfite and air-saturated data). Matching can be done by linearly adjusting the sensor output so that $pO_2[\varphi,T_s] = A + B \times pO_2[\varphi,T_s]$, using offset-adjust, $A$ [dimensionless], and gain, $B$ [dimensionless], terms. Alternatively, as the manual recommends, the adjustment can be applied to the phase term, such that $pO_2[\varphi,T_s] = pO_2[A + B \times \varphi, T_s]$. Slight differences between the two approaches can be expected.

Note that, ideally, the two-point calibrations will be performed at $T = T_s$. This can be done in a water bath (to keep temperature constant) with two separate beakers. The first beaker is gently bubbled with air to equilibrate it. When the 100% air-saturated reading is made, the optode can be transferred to the beaker containing sodium sulfite which is also at the same temperature. Note that the sulfite reaction with oxygen is exothermic, so cooling the solution to the ambient waterbath temperature is required, as is limiting exposure to air.

This step is not necessary if advanced multi-point calibration data is used since the multi-point calibration data use three Winkler calibrated reference optodes.

**Summary of procedure**

The following list of steps summarizes how to calibrate an Aanderaa optode using the new method and which of the 10 coefficients (see summary in Table 1) are determined at each step in the procedure:

Step 1: Determine the two anoxic-foil coefficients $\tau_o'$ and $E_{\tau o}$ by fitting Eq. 8 to zero oxygen calibration data, then interpolate for setpoint values of $\tau_o$ ($T_c$) and calculate values of $\tau_o$ ($T_c$)/$\tau$ ($T_c$).

Step 2: Determine the three oxic-foil coefficients $K_{SV1}(T_c)$, $K_{SV2}(T_c)$, and $f_{01}(T_c)$ by fitting Eq. 6 to results from Step 1, then determine the four Arrhenius fit coefficients $K'_{SV1}$, $K'_{SV2}$, $E_{SV1}$, and $E_{SV2}$ using the form of Eq. 11.

Step 3: Check for any simplification of the general solution Eq. 7 based on results of Step 2. For example, if $f_{01}(T_c)$ is nearly independent of temperature, then set as constant. If $\beta >> 1$,

**Table 1.** The ten calibration coefficients (highlighted), their relation to primary model quantities, and a brief description of their physical meaning. Note that if β is used, then $K'_{SV2}$ and $E_{SV2}$ are not required, so nine coefficients are required. If multi-point calibration data are used, then $A = 0$ and $B = 1$, bringing the number of coefficients down to seven.

| Primary coefficient | Secondary coefficient | Physical interpretation [units] |
|---|---|---|
| $f_{01}$ | $\boldsymbol{f_{01}}$ | Fraction of unquenched fluorophores responding with the more accessible Site 1 quenching characteristics [dimensionless] |
| $K_{SV1}$ | $\boldsymbol{K'_{SV1}}$ | Site 1 amplitude term [mbar$^{-1}$] |
| | $\boldsymbol{E_{SV1}}$ | Site 1 activation energy [J mol$^{-1}$] |
| $K_{SV2}$ | $\boldsymbol{K'_{SV2}}$ | Site 2 amplitude term [mbar$^{-1}$] |
| | $\boldsymbol{E_{SV2}}$ | Site 2 activation energy [J mol$^{-1}$] |
| $\tau_o$ | $\boldsymbol{\tau_o'}$ | Fluorescence lifetime amplitude [s] |
| | $\boldsymbol{E_\infty}$ | Minimum energy of fluorophores required for self-quenching in the absence of oxygen; determined temperature response of $\tau_o$ [J mol$^{-1}$] |
| Θ | **Θ** | Reduction in quenching efficiency due to hydrostatic pressure for Site 1 and Site 2 [dimensionless] |
| $A$ | $\boldsymbol{A}$ | Offset-adjust, no meaning [dimensionless] |
| $B$ | $\boldsymbol{B}$ | Gain adjust, no meaning [dimensionless] |
| β | $K_{SV1}/K_{SV2}$ | Ratio of quenching amplitudes at Site 1 to Site 2. Note this is not one of the ten fundamental coefficients [dimensionless] |

consider eliminating second-order terms in Eq. 9. Repeat Step 2 based on these simplifications.

Step 4: Choose an appropriate value for $T_s$ then use Eq. 9 to calculate an isothermal calibration curve for $pO_2(T_s)$, and Eq. 12a,b to scale to other temperatures.

Step 5: If the standard factory calibration sheets were used, apply results of a two-point calibration (i.e., sulfite zero and air-saturated) performed at $T_s$ to the results of Step 4 to determine the two offset- and gain-adjust coefficients $A$ and $B$ as described in Section Two-point calibration above. If multi-point calibration data were used, there is no need to correct the calibration coefficients so set $A = 0$ and $B = 1$. You now have a laboratory-calibrated optode.

Step 6: If analyzing field data, additional matching to in situ Winklers can be performed using the same procedure in Step 5 by applying Eq. 13. Ideally, however, field Winkler data would be added to the laboratory calibration data set, which may include multipoint laboratory Winkler data, before performing regression fits for calibration equation coefficients. One can also consider preferentially weighting the field data over the laboratory data in the regression fits. The pressure correction term, Θ, can assumed to be a constant value of Θ = 0.7965 to agree with the results of Uchida et al. (2008), or it can be calculated as part of the regression fit.

**Curve fitting**

A robust nonlinear least-squares regression algorithm (Mathworks Inc., Matlab function fit.m with least absolute residuals, 'LAR', option enabled) is used for curve fitting. Errors in fits are taken as the 95% confidence intervals.

## Assessment

**Standard factory calibration data**

We first assess the calibration equation by applying it to standard foil calibration data that is supplied with every optode even though, as stated previously, it is known that factory-delivered optodes normally read low relative to true at the time of delivery from the factory. We chose this approach because users can then easily apply the new calibration equation to their own standard factory data sheets. Typical factory calibration data are shown in Fig. 1 plotted as either phase (Fig. 1a), or lifetime (Fig. 1b) calculated using Eq. 5. We measured $f_m$ = 4.997 ± 0.006 kHz for one optode (s/n 382) using an oscilloscope.

We note that Uchida et al. (2008) assumed a linear temperature dependence of $\varphi_o(T)$, even though a much better approximation is a second-order polynomial as shown by the dashed line in Fig. 1a. Because of this, we feel that Uchida et al. (2008) actually needs another temperature-dependent coefficient, which interestingly would bring their total number of coefficients up to ours. We see that assuming a linear dependence of $\tau_o(T)$, rather than a linear dependence of $\varphi_o(T)$, would provide a much better empirical fit. Sinaasappel and Ince (1996) chose to fit $\tau_o(T)$ using a second-order polynomial, which at least for this foil seems unnecessary since a linear fit would suffice. Regardless, neither of these empirical relationships produces coefficients that can be interpreted by any standard theory, which is why we chose to fit to an Arrhenius relationship.

**Step 1: Arrhenius fit to zero oxygen calibration data**

Table 2 presents a summary of Arrhenius fits to zero oxygen calibration data from 24 manufacturer calibration sheets. The selection covers a large range of calibration dates, foil types, and includes calibrations performed using the same foil on a different sensor and multi-point data. Corresponding Arrhenius plots are shown in Fig. 2a and decay rates $1/\tau_o$ in Fig. 2b. A statistical analysis of all foil responses found $1/\tau_o'$ = 48239 (± 7607, or 16%) [s$^{-1}$] and $E_{\tau o}$ = 3055 (± 841, or 28%) [J mol$^{-1}$]

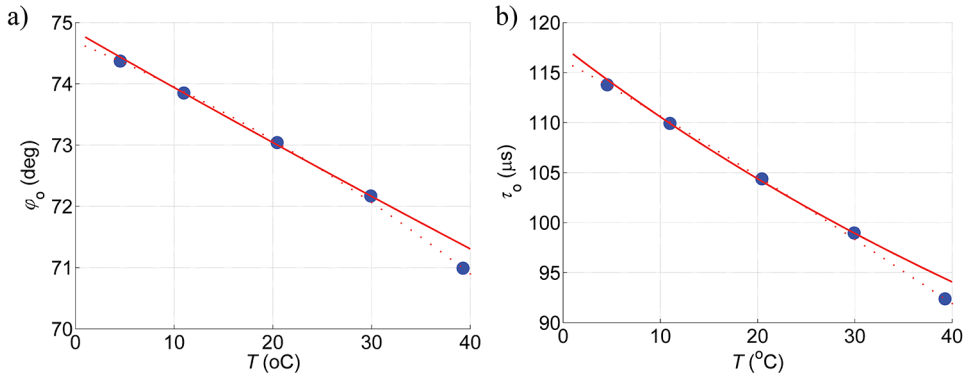


**Fig. 1.** Temperature dependence of foil #1707 showing: a) raw phase at zero oxygen ($\varphi_o$) and b) lifetime at zero oxygen ($\tau_o$) calculated using Eq. 5. In both plots, manufacturer calibration data are shown (blue dots) along with curves that use an Arrhenius fit (red solid lines) to the decay rate $1/\tau_o$ in Fig. 1b, and an empirical quadratic curve fit (red dotted line) to $\varphi_o(T)$ in Fig. 1a.

**Table 2.** Results of analysis of 24 manufacturer calibration sheets using Eq. 8, showing Column 1—sequence identification number (*ID*) that corresponds with Fig. 2; Column 2—manufacturer's identification number, with following notation 'N' for normal factory data sheets for use on model 3830/3835 sensors, 'E' for use on model 4330 sensors, 'EM' advanced multipoint calibrations with superscript 'a' and 'b' to identify two multipoint calibrations using foils with same manufacturer's ID but on different model 4330 sensors and corresponding to green data points in Fig. 2c; and 'F' for fast response foils with no overcoat; Column 3—calibration date; Column 4—Fluorescence rate amplitude; Column 5—Arrhenius activation energy. Highlighted in bold are the three oldest foils with sequence *ID* = [1, 8, 14] and corresponding to blue data points in Fig. 2c. Our model foil is sequence *ID* = 9.

| Seq. *ID* | Manuf. ID | Date | $1/\tau_o'$ [$s^{-1}$] | $E_{\tau o}$ [J $mol^{-1}$] |
|---|---|---|---|---|
| **1** | **0804N** | **21-Feb-2004** | **37726** | **1946.9** |
| 2 | 1023N | 18-Aug-2010 | 39573 | 3265.4 |
| 3 | 1023E | 23-Aug-2010 | 41856 | 2232.1 |
| 4 | 1206E | 13-Aug-2012 | 44999 | 2453.8 |
| 5 | 1206EM[a] | 23-Jun-2013 | 40516 | 2114.7 |
| 6 | 1206EM[b] | 23-Jun-2013 | 45077 | 2387.0 |
| 7 | 1207F | 13-Aug-2012 | 45208 | 2447.5 |
| **8** | **1403N** | **17-Jun-2003** | **42821** | **2268.3** |
| 9 | 1707N | 22-Jun-2007 | 48826 | 3969.5 |
| 10 | 2408N | 28-Aug-2009 | 50858 | 3972.2 |
| 11 | 2408N | 04-Mar-2009 | 52079 | 4064.1 |
| 12 | 2408E | 13-Aug-2009 | 50704 | 2678.2 |
| 13 | 2808F | 02-Dec-2008 | 45643 | 2421.1 |
| **14** | **3603N** | **12-Sep-2003** | **41989** | **2185.0** |
| 15 | 3606N | 19-Sep-2006 | 51650 | 3865.2 |
| 16 | 4104N | 13-Nov-2004 | 69141 | 4032.0 |
| 17 | 4804N | 25-Jul-2006 | 55011 | 3627.3 |
| 18 | 4807N | 30-May-2008 | 54061 | 4203.3 |
| 19 | 4807E | 22-Oct-2008 | 44289 | 2318.1 |
| 20 | 4902N | 25-Jul-2006 | 50417 | 2653.6 |
| 21 | 4909N | 08-Feb-2010 | 60324 | 4277.9 |
| 22 | 4909E | 05-Feb-2010 | 43081 | 2290.5 |
| 23 | 5005N | 09-Feb-2006 | 41559 | 3365.2 |
| 24 | 5009N | 02-Jun-2010 | 60324 | 4277.9 |

based on mean and standard deviation of Columns 4 and 5 from Table 2. In particular, our model foil #1707N had $1/\tau_o' = 4.8826\times10^4$ [$s^{-1}$] and activation energy $E_{\tau o} = 3.9695\times10^3$ [J $mol^{-1}$]. This curve is also reproduced in Fig. 1, identified as solid red lines.

Temperature normalized ($T$ = 20 °C) Arrhenius plots are

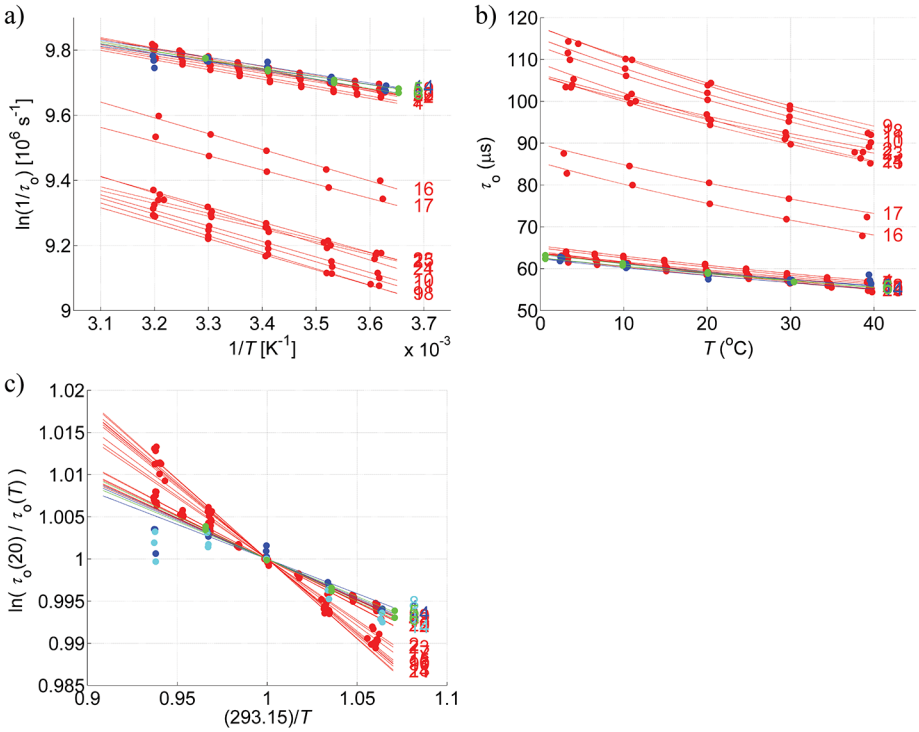


**Fig. 2.** Temperature dependence of multiple foils under anoxic conditions, showing a) Arrhenius plots of decay rate $1/\tau_o$ with linear fits where the slope is proportional to the activation energy; b) the corresponding best line fits for lifetime, and c) same as (a) but normalized by interpolated values at $T$ = 20°C using best line fits. Manufacturer calibration data (dots) are fitted using Eq. 8. See Table 2 for description of calibration information based on identifier number (*ID* is located to right at end of each line fit). Data are color coded as follows: calibrated before (blue) and after (red) March 2014; advanced multi-point calibrations in 2013 for two sensors (green); normalized using nearest setpoint data (cyan), which fall within $T$ = 20 ± 0.5°C.

shown in Fig. 2c. Data for the three oldest foils, calibrated before March 2004, are highlighted (colored blue in Fig. (2c) and shown using bold text in Table 2). These older foils show a distinct downwards curvature of the Arrhenius plots at higher temperatures ($T$ > 30°C), implying that the fluorophore deactivation rate decreases with increasing temperature for these foils. Foil with sequence *ID* = 1 (see Column 1 or Table 1) actually has a negative activation energy since the slope becomes positive. Such a response can occur by any denaturing process, which would presumably alter the foil's fluorescence properties irreversibly. It can also occur if the energetics of the fluorophore/foil interaction can be described by a 'potential well', which has no initial energy barrier to overcome and higher reaction rates at lower kinetic energies.

**Step 2: Fit to nonlinear Stern-Volmer equation**

Stern-Volmer plots of the factory calibration data for our model foil #1707N are presented in Fig. 3. Better linearity of the phase ratio (Fig. 3a) persuaded Uchida et al. (2008) to work with phase rather than lifetime (Fig. 3b) since, they argued, the end result of a calibration procedure is a linear sensor. This approach, although reasonable for calibration purposes, eliminates most of the underlying theoretical insight in the foil's physical properties that can be extracted from the problem.

We determine the three foil calibration coefficients $K_{SV1}$, $K_{SV2}$, and $f_{01}$ by fitting the isothermal factory calibration data to Eq. 6. Best fit values of the coefficients are: $K_{SV1}$ = 48.9 × $10^{-3}$ (±0.0088) [mbar$^{-1}$], $K_{SV2}$ = 2.11×$10^{-3}$ (±0.00035) [mbar$^{-1}$], and $f_{01}$ = 0.819 (±0.015), numbers in parentheses are standard deviations ($N$ = 5 different calibration temperatures, covering range $T$ = 5°C –40°C). These results, which are typical based on literature values, indicate that approximately 82% of the foil responds with type 1 site characteristics whereas only 18% responds with type site 2 characteristics. The quenching at type site 1 is more efficient than at type site 2 by a factor $K_{SV1}/K_{SV2}$, or approximately 23.2 ± 8.0.

By applying the same analysis to all N-type foils, we obtain the results presented in Table 3. The three oldest foils (highlighted in bold text) have the lowest $K_{SV1}$ values. In addition, one foil (sequence *ID* = 20) had an outlying $f_{01}$ coefficient more than three standard deviations lower than the mean of all 15 foils. Excluding sequence *ID* = [1, 20], the variability of the three coefficients $K_{SV1}$, $K_{SV2}$, and $f_{01}$ expressed as percentage standard deviations from mean values are 20%, 32%, and 3%, respectively. This finding implies that $K_{SV2}$ and $K_{SV1}$ primarily determine variability in response between different optodes.

The effect of increasing foil temperature on the optode's response is evident from the different isothermal curves in Fig. 3b.

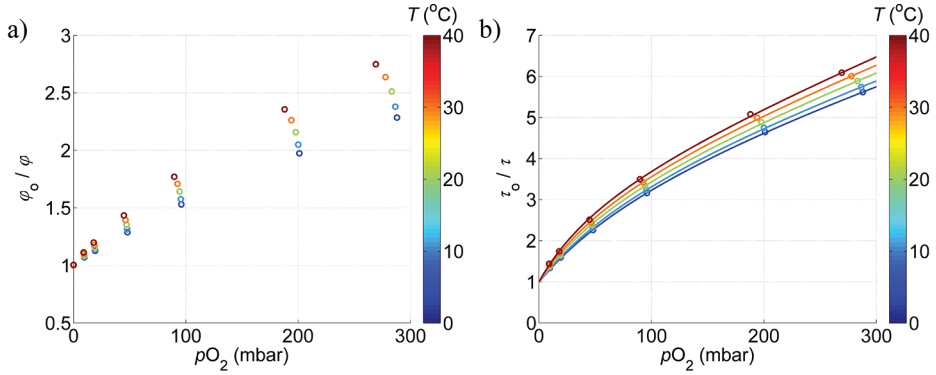


**Fig. 3.** Factory calibration data (circles) for foil #1707, presented as a) phase measurements and b) fluorescence lifetime. Lifetime and phase are related using Eq. 5. The solid lines in Fig. 1b are regression fits to a two site nonlinear Stern-Volmer model described by Eq. 6.

**Table 3.** Mean values of the three coefficients used in the two-site model, derived by fitting all 15 'N' type (see Table 2, Column 2) manufacturer calibration sheet data to Eq. 6. Estimates are the mean of 5 values calculated for each set-point temperature. Column 1 is the sequence identification number (*ID*), and the highlighted rows correspond to the three oldest foils as in Table 2. See Table 1 for a description of the three foil coefficients presented in Columns 2–4. Sequence *ID* = 20 (italicized) is a potential outlier with anomalously low $f_{01}$ coefficient.

| Seq. *ID* | $K_{SV1}$ (× $10^{-3}$) [$mbar^{-1}$] | $K_{SV2}$ (× $10^{-3}$) [$mbar^{-1}$] | $f_{01}$ |
|---|---|---|---|
| **1** | **30.52** | **2.16** | **0.802** |
| 2 | 48.88 | 2.87 | 0.798 |
| **8** | **28.53** | **2.1** | **0.797** |
| 9 | 48.9 | 2.11 | 0.819 |
| 10 | 38.27 | 1.14 | 0.866 |
| 11 | 39.97 | 1.14 | 0.863 |
| **14** | **25.33** | **1.99** | **0.802** |
| 15 | 43.16 | 1.8 | 0.839 |
| 16 | 31.57 | 2.69 | 0.85 |
| 17 | 36.11 | 2.87 | 0.847 |
| 18 | 39.84 | 1.32 | 0.857 |
| *20* | *46.05* | *4.04* | *0.647* |
| 21 | 48.92 | 2.72 | 0.805 |
| 23 | 39.51 | 1.51 | 0.852 |
| 24 | 48.92 | 2.72 | 0.805 |

**Step 3: Temperature dependence of coefficients**

The temperature dependence of the three foil calibration coefficients $K_{SV1}$, $K_{SV2}$, and $f_{01}$, described above are shown in Fig. 4a. It is found that $f_{01}$ is nearly constant, and that $K_{SV1}$ is most sensitive to temperature as we might expect. The value of β varies by < 8% over the temperature calibration range (0°C –40°C). An Arrhenius plot of $K_{SV1}$ (Fig. 4b) shows a near straight line providing evidence that the temperature dependence of the bimolecular interaction between the fluorophore and oxygen quencher obeys this law equally well. The best fit to Eq. 11 has pre-exponential factor $K_{SV1}' = 2.11$ [$mbar^{-1}$] and activation energy $E_{SV1} = 9.21 \times 10^3$ [J $mol^{-1}$].

We now impose a constant mean value of $f_{01} = 0.82$ and recalculate the temperature dependency of $K_{SV1}$ and $K_{SV2}$. The results are shown in Fig. 5a. The corresponding Arrhenius plots for $K_{SV1}$ and $K_{SV2}$ are show in Fig. 5b,c, respectively. Because we are now determining two coefficients from the same data set, rather than three, the confidence intervals are reduced, but this disguises the fact that we have introduced uncertainty into the formulation by imposing a constant value for $f_{01.}$ It is now evident that $K_{SV2}$ is also well described by an Arrhenius equation but with lower activation energy than that for $K_{SV1}$.

Since $f_{01}$ and β are nearly constant and independent of temperature, we take these as constants to yield the results shown in Fig. 6. With more analysis, it may be necessary to account for the variability in $f_{01}$ and β with additional calibration coefficients.

**Step 4: Isothermal calibration curves**

We first check the general solution Eq. 7, which forms the basis of the new calibration equation. Results are plotted in Fig. 7a using fits to the three foil coefficients shown in Fig. 4a. Agreement between the curves and the raw data (open circles) verify the solution is correct. Note that the sensor is more sensitive at lower oxygen levels. Also, even in the absence of oxygen the foil has a significant thermal response. The decrease of approximately 4 degrees of phase under anoxic conditions over the 40°C calibration range (see lower right of Fig. 7a) is equivalent to the quenching that would be associated with increasing oxygen partial pressure to approximately 5–10 mbar.

The sensor calibration curves shown in Fig. 7a are only partially temperature compensated by an empirical relationship for $\tau_o(T)$. We choose a reference temperature of $T_s = 20.44$°C corresponding to the mid-range setpoint temperature of the factory calibration data. The results of applying the new calibration equation (Eq. 12a,b) to an optode using foil #1707N are shown in Fig. 7b. We assess the goodness of fit by calculating the difference of the predicted $pO_2$ using the calibration

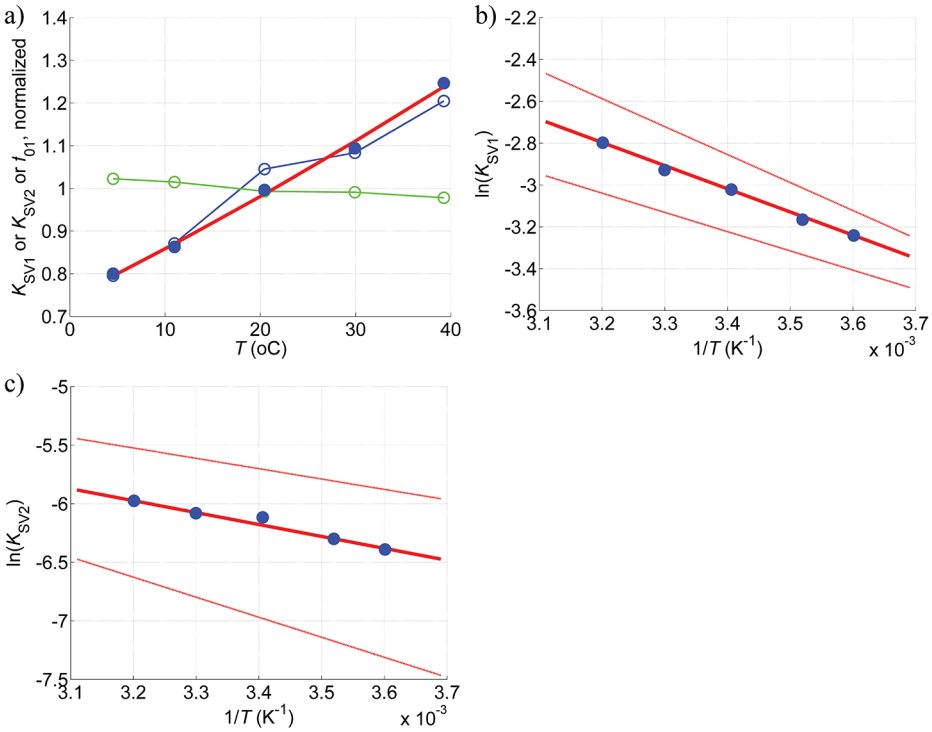


**Fig. 4.** Temperature response of the three calibration coefficients for foil #1707, showing (a) coefficients $K_{SV1}$ (blue dots) and rescaled Arrhenius fit (thick red line) from Fig. 4b, $K_{SV2}$ (blue circles and thin blue line), and $f_{01}$ (green circles and thin green line), where coefficients are normalized by their mean values; b) Arrhenius plot of $K_{SV1}$ (blue dots) and best fit (thick red line) of Eq. 11, with ± 95% confidence intervals (thin red lines); c) same as (b) except for $K_{SV2}$.

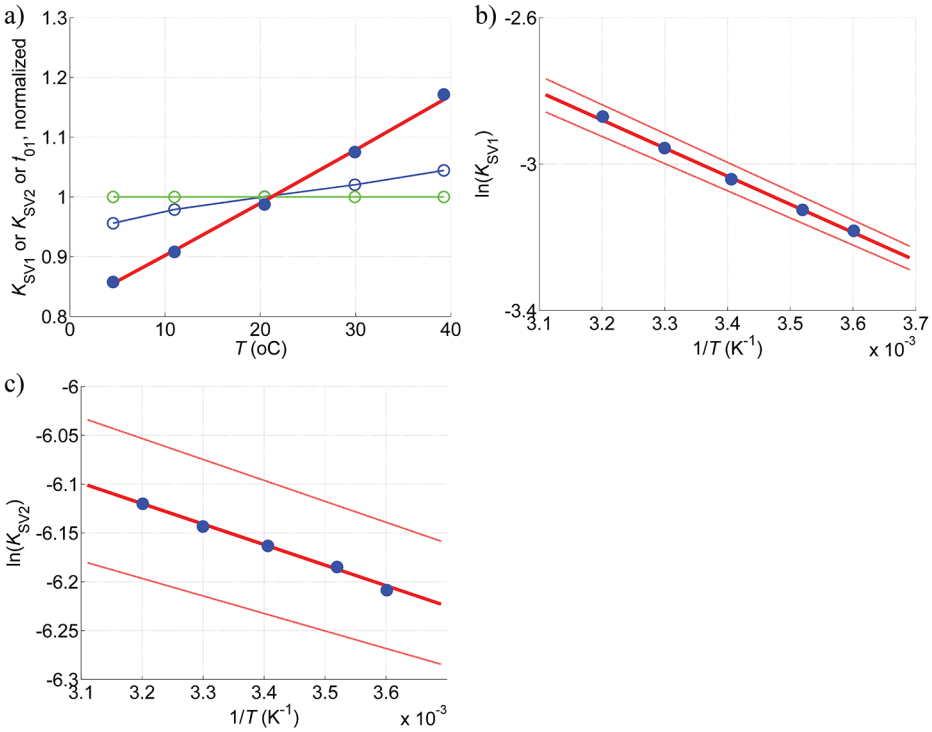


**Fig. 5.** Same as Fig. 4, except $f_{01}$ is set to a constant value.

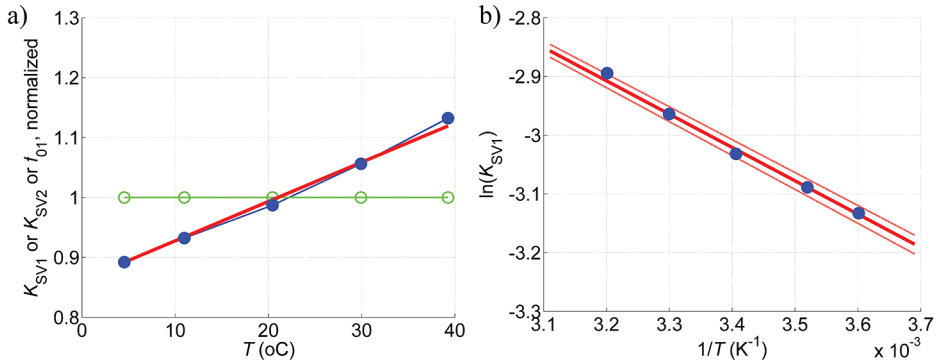


**Fig. 6.** Same as Fig. 4 except $f_{01}$ and β are set to constant values.

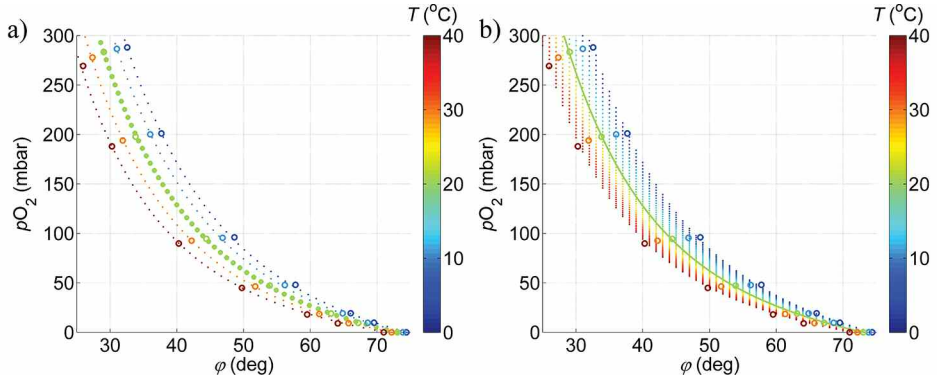


**Fig. 7.** Isothermal calibration curves for foil #1707, calculated using (a) Eq. 7 and the three-foil parameters derived from the curve fits in Fig. 3b (shown as dotted lines) and (b) Eq. 12 at a reference temperature $T_s$ = 20.44°C (shown as central green line), and different temperatures and discrete values of φ (shown as points falling along vertical lines). Also shown are the factory calibration data (circles).

model and the factory calibration data. As expected, the best fit is obtained using the raw calculated foil coefficients presented in Fig. 4, the mean error is –0.12 ± 1.1 [mbar]. For consistency, we used an Arrhenius fit to $f_{01}(T)$ for this calculation. Similar analysis of the foils from Table 3, excluding sequence *ID* = [1, 20] as possible outliers, totaling 455 individual calibration points over a temperature range of 5°C–40°C, yielded mean errors of –0.57 ± 1.48 [mbar]. The fit degrades as further approximations are introduced; the mean error for the choice of foil coefficients shown in Fig. 6 is 0.18 ± 1.5 [mbar]. The results for our model sensor are summarized in Table 4.

**Advanced multi-point factory calibration data**

Since Fall 2012, Aanderaa has offered users, at additional expense, their own multi-point calibration service, which is performed at their factory in Norway. The sensors are placed in a temperature-controlled water bath at various set-points and calibrated against three secondary-standard optodes regularly calibrated against primary Winkler titration samples using an automatic titrator from SI Analytics (see information sheet by Tengberg and Hovdenes 2013). Using nitrogen as a carrier gas, the oxygen content of the water bath is controlled by mass flow controllers. The multi-point calibration service provides a very thorough laboratory calibration data set which includes 1) raw calibration data; 2) seven calibration coefficients calculated using the linear Stern-Volmer calibration equation of Uchida et al. (2008); and 3) post-calibration validation measurements that are independent of the calibration data set. Two brand new optodes were calibrated using the advanced multi-point calibration service on 23 June 2013.

Since the multi-point calibration service does not calibrate using a sodium sulfite zero point, some interpolation is required to determine the zero-point phase calibration from their near zero calibration data (the errors incurred in interpolation are small since the calibration data are within a few micro-molar of zero). Residuals for the Uchida et al. (2008) fit and fits to our new calibration equation are shown in Fig. 8 and summarized in Table 5. It is clear for these two optodes that the Uchida et al. (2008) calibration equation has significantly smaller residuals than the new calibration equation. The manufacturer also provides validation data for the optode after calibrating it. This provides a true test of the calibrated optode from which the manufacturer has developed a specification of accuracy, which is stated to the greater of 2.5 μmol kg$^{-1}$ or 1.5% of the reading. These specifications are drawn on Fig. 8 for comparison and fall outside the range of residual errors derived using our new calibration equation.

**Table 4.** Goodness of fit for a model sensor calibrated using the standard factory supplied calibration data set and the new calibration equation (Eq. 12), for the three cases presented in Figs. 4–6. Means and standard deviations are calculated for all 35 setpoints, which cover a temperature range of 5°C–40°C and $pO_2$ range of 0–270 mbar.

| Corresponding fig. | Mean [mbar] | Std [mbar] |
|---|---|---|
| 4 | –0.1208 | 1.1207 |
| 5 | –0.6176 | 1.1545 |
| 6 | 0.1811 | 1.4699 |

**Table 5.** Comparison of goodness of fits of two calibration equations to Aanderaa multi-point calibration data taken on 23 June 2013 for two brand new optodes.

| Sensor s/n | Calibration equation | Mean [mbar] | Std [mbar] |
|---|---|---|---|
| 1221 | Eq. 12, constant $f_{01}$ | 0.1452 | 0.8542 |
| | Uchida et al. (2008) | –0.0198 | 0.1488 |
| 1222 | Eq. 12, constant $f_{01}$ | 0.1735 | 0.8572 |
| | Uchida et al. (2008) | 0.0039 | 0.0668 |

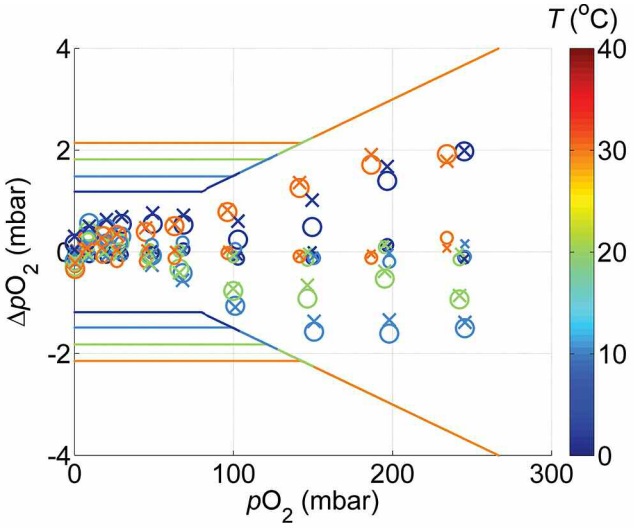


**Fig. 8.** Residual calibration errors ($\Delta pO_2$) as a function of oxygen partial pressure ($pO_2$) and temperature ($T$), derived using advanced multi-point factory calibration data for two brand new optodes: s/n 1221 (circles) and s/n 1222 (crosses). Calculations were made using either Eq. 12 with constant $f_{01}$, shown by large symbols, or the factory-derived calibrations following Uchida et al. (2008), as shown by small symbols. The colored straight lines demarcate the manufacturer's quoted accuracy, based on whichever is the greater of ± 2.5 μmol $O_2$ $kg^{-1}$ and ±1.5%, noting that the lower $O_2$ limit varies with temperature.

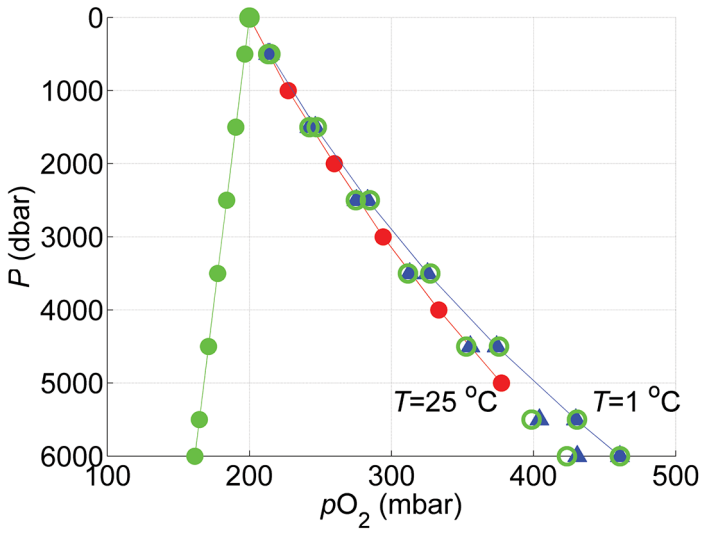


**Fig. 9.** Pressure compensation of an optode. Uchida et al. (2008) predicts a decrease in optode reading from assumed initial surface reading of 200 mbar at 3.2% per 1000 dbar (green dots). Klots (1961) predicts an increase in oxygen reading (red dots) based on laboratory measurements of oxygen solubility at $T$ = 25°C for $P$ = 0 – 5000 dbar. Recalculated profiles for Uchida et al. (2008) using Eq. 13 calibrated for the deep cold ocean by setting Θ = 0.7965 (green circles) agree with our predicted increase in optode reading based on Eq. 13 with Θ = 1 (blue triangles) to within ± 0.6% over the ranges $P_w$ = 0 – 6000 dbar at $T$ = 1°C and $P_w$ = 0 – 3900 dbar at $T$ = 25°C.

### Pressure compensation

Shown in Fig. 9 are example calculations of how calibrated optode readings would change with hydrostatic pressure according to Uchida et al. (2008) (green curves) and Eq. 13 (red and blue curves). It is clear that an optode recalibrated using our new procedure would read significantly higher $fO_2$ deep in the ocean than the same optode calibrated using the Uchida et al. (2008) formula. This is potentially confusing so we explain it in greater detail. The Uchida et al. (2008) formula will not provide an in situ reading of $fO_2$, rather it will provide a reading analogous to a 'potential' $fO_2$ reading, meaning the optode reading will be referenced to the sea surface. This is because the Uchida et al. (2008) calibration equation does not specify a decreasing Henry's Law solubility with increasing hydrostatic pressure. Uchida's pressure compensation makes the sensor read uniform oxygen saturation levels, regardless of depth, assuming all other water properties, including temperature, salinity, and dissolved oxygen concentration are constant. Since our calibration equation includes hydrostatic pressure dependence to the Henry's Law oxygen solubility coefficient, a sensor calibrated using Eq. 13 will read the in situ oxygen fugacity, or activity, that a fish deep in the ocean would experience. This reading is higher than a sensor calibrated without a pressure dependent Henry's Law coefficient. However, since oxygen solubility decreases with hydrostatic pressure according to Henry's Law, if all other water properties are constant the optode calibrated using Eq. 13 will also read depth invariant oxygen saturation levels.

Small errors are introduced by calibrating Eq. 13, which is essentially based on Klots (1961) data at STP, to the deep cold ocean due to the non-linearity of Eq. 13 in $T$ and $P$. From Eq.

14, setting $\Theta = 0.7965$ in Eq. 13 introduces an uncertainty in calculated $fO_2$ of ± 0.6% over the range $P_w = 0 – 6000$ dbar at $T = 1$°C, as shown in Fig. 9. Similar agreement is found at $T = 2$°C but over the more limited range of $P_w = 0 – 3900$ dbar. The uncertainty increases to a maximum value of ± 1.7% at $P = 6000$ dbar and $T = 25$°C. However, since no deep waters in the ocean are this warm, for oceanographic applications the error is ± 0.6%. It is possible this uncertainty could be reduced further if $\Theta$ is included as a variable when fitting field data.

## Discussion

We have presented a new calibration equation for an Aanderaa Inc. dissolved oxygen optode. The calibration equation is derived based on a two site nonlinear Stern-Volmer model for fluorescence quenching. This model conceptualizes that fluorophores embedded in the foil matrix occupy one of two distinct regions with type site 1 characteristics being more accessible to diffusion oxygen molecules than those in type site 2 regions. We have outlined additional steps that are necessary to match the resulting laboratory calibrated optode to in situ Winkler data and compensate for known hydrostatic pressure dependence. Table 1 provides a summary of the ten coefficients used in the calibration equation, eight of which have a physical meaning.

We have first assessed the method using original factory calibration data for the foils since these data are supplied with every optode at delivery. Table 4 provides a summary of the goodness of fit for a model sensor-calibrated using the new calibration equation. We know that the foils are calibrated at a third-party factory, not at the Aanderaa factory, and that these calibrations can differ by more than 10% from the two-point calibrations performed at the Aanderaa factory before sensor delivery. We cannot say why raw factory foil calibration data alone cannot be used to calibrate an optode and requires a second two-point calibration, other than to suggest one of two possibilities: 1) drift in the factory's calibration occurs between when the foil is manufactured and when it is installed on an optode and the two-point calibration performed, or 2) there is a fundamental measurement offset between the production optode and the instrumentation used to calibrate the foil. Addressing the first possibility, we know that sensor calibrations do indeed drift with a combination of infrequent usage and long-term storage. D'Asaro and McNeil (2013) observed calibration drift of several optodes over a period of several years that was well described by a single decaying exponential with a decay constant of approximately 2 years and an amplitude of 28%. It is, therefore, possible that the foil's calibrations change from the time they were first manufactured and calibrated to when they were first installed on the optodes and two-point calibrated at the Aanderaa factory. Perhaps a statistical analysis of many more optode calibration sheets will shed light on this problem. This is highly relevant to the oceanographic community because there are several hundred irrecoverable Argo floats that have been deployed on ships of opportunity whose only calibrations are the factory foil and two-point data.

We have also assessed the method using multi-point factory calibration data which is now offered as an advanced service by Aanderaa. Each optode is individually calibrated during a batch run against three Winkler maintained secondary standards. Alternatively, users can, at considerable effort, set up their own laboratory multi-point calibration system (Bittig et al. 2012) to obtain the necessary laboratory calibration data. Multi-point calibration data eliminate uncertainty associated with third-party foil calibrations and remove the need for standard 'two-point' calibrations, which removes the need for two calibration coefficients with no physical meaning (see Table 1, coefficients $A$ and $B$). Table 5 provides a summary of the goodness of fit for two model sensors calibrated using the new calibration equation and compares these results to the Uchida et al. (2008) formulation. Not surprisingly, the Uchida et al. (2008) formulation, which uses polynomial fits to best match to the calibration data rather than functional forms imposed by theory, does a better job at matching the sensor output to the calibration data. Application of the new calibration equation provides two calibrated sensor that fall within the manufacturer's specifications.

We have not reported an assessment of our calibration equation against field data nor addressed how the various coefficients change with time, although these are the obvious next steps. Users will need to determine how best to modify the procedure to incorporate their field data. There are many factors involved. First and foremost, one must decide what, if any, calibration data from the factory should be retained in the method. As indicated from our assessment, we suspect that the most valuable information available from the factory calibration sheets is the zero oxygen phase measurements since these measurements are more likely to be immune to aging effects (e.g., photo-degradation and possibly ozone destruction). The decision on which factory data to keep will also depend on the relative quality of the laboratory calibration and the field data. Although it is highly desirable to supplement any laboratory calibrations of optodes with in situ Winkler calibrations made near the expected operating temperature; sometimes this is not practical. For example, in our studies of air-sea gas exchange in hurricanes using air-deployed floats, factory calibrations of optodes were supplemented with in situ Winkler data obtained in much colder waters of Puget Sound than those under a hurricane (D'Asaro and McNeil 2013). Because we were using only a few optodes, we used the same foil on all the optodes since this makes tracking calibration amongst the optodes easier. We recommend other users consider this same tactic where intercalibrations amongst a set of optodes is important.

A statistical analysis of a significant number (24) of optodes for which we were able to obtain factory calibration data sheets identified one optode as having a negative Arrhenius activation energy associated with fluorophore self-quenching

in the absence of oxygen at $T > 30$°C. This provides some caution to users to prevent overheating of optode foils, since it is seems reasonable this could lead to irreversible change in the foil's response for heat sensitive foils. A second optode was identified as having an anomalously low $f_{01}$ coefficient relative to 14 other similar model optodes. This demonstrates one of the important consequences of having a calibration equation with coefficients that relate directly to meaningful characteristics of the sensor response. Analysis of 13 similarly calibrated foils shows that the site 2 and site 1 Stern-Volmer coefficients vary significantly, 32% and 20% respectively, whereas the fraction of each site remains relatively constant, varying by only 3%. If optode drift is the result of foil-aging processes, then we might similarly expect foils to age by altering the Stern-Volmer constants for one of the sites, rather than altering the fraction of each site. Identifying changes in calibration coefficients over time with sensor use and attributing those changes to a physical characteristic of the sensor was a primary motivator for this effort and will be the focus of future work.

## References


Bailey, E. A., and G. K. Rollefson. 1953. The determination of the fluorescence lifetimes of dissolved substances by a phase shift method. J. Chem. Phys. 21(8):1315 [doi:10.1063/1.1699212].

Bittig, H. C., B. Fiedler, T. Steinhoff, and A. Körtzinger. 2012. A novel electrochemical calibration setup for oxygen sensors and its use for the stability assessment of Aanderaa optodes. Limnol. Oceanogr. Methods 10:921-933 [doi:10.4319/lom.2012.10.921].

Boyer, T. P., J. I. Antonov, O. K. Baranova, H. E. Garcia, D. R. Johnson, R. A. Locarnini, and S. Levitus. 2009. World ocean database 2009. NOAA Atlas NESDIS, 66.

Bushinsky, S. M., and S. Emerson. 2013. A method for in-situ calibration of Aanderaa oxygen sensors on surface moorings. Mar. Chem. 155:22-28 [doi:10.1016/j.marchem.2013.05.001].

Carey, F. G., and Q. H. Gibson. 1976. The activity of dissolved oxygen at 1000 atm hydrostatic pressure. Deep Sea Res. Oceanogr. Abstr. 23(12):1215-1216 [doi:10.1016/0011-7471(76)90898-6].

Carraway, E. R., J. N. Demas, B. A. DeGraff, and J. R. Bacon. 1991. Photophysics and photochemistry of oxygen sensors based on luminescent transition-metal complexes. Anal. Chem. 63(4):337-342 [doi:10.1021/ac00004a007].

Culberson, C. H., and S. Huang. 1987. Automated amperometric oxygen titration. Deep Sea Res. A 34(5):875-880 [doi:10.1016/0198-0149(87)90042-2].

D'Asaro, E., and C. McNeil. 2007. Air–sea gas exchange at extreme wind speeds measured by autonomous oceanographic floats. J. Mar. Syst 66(1):92-109 [doi:10.1016/j.jmarsys.2006.06.007].

———, and ———. 2013. Calibration and stability of oxygen sensors on autonomous floats. J. Atmos. Oceanic Technol. 30:1896-1906 [doi:10.1175/JTECH-D-12-00222.1].

Demas, J. N., B. A. DeGraff, and W. Xu. 1995. Modeling of luminescence quenching-based sensors: comparison of multisite and nonlinear gas solubility models. Anal. Chem. 67(8):1377-1380 [doi:10.1021/ac00104a012].

———, B. A. De Graff, and P. B. Coleman. 1999. Oxygen sensors based on luminescence quenching. Anal. Chem. 71(23):793-800 [doi:10.1021/ac9908546].

Emerson, S., and C. Stump. 2010. Net biological oxygen production in the ocean—II: Remote in situ measurements of $O_2$ and $N_2$ in subarctic pacific surface waters. Deep Sea Res. I 57(10):1255-1265 [doi:10.1016/j.dsr.2010.06.001].

Enns, T., P. F. Scholander, and E. D. Bradstreet. 1965. Effect of hydrostatic pressure on gases dissolved in water. J. Phys. Chem. 69(2):389-391 [doi:10.1021/j100886a005].

Fiedler, B., P. Fietzek, N. Vieira, P. Silva, H. C. Bittig, and A. Körtzinger. 2012. In situ $CO_2$ and $O_2$ measurements on a profiling float. J. Atmos. Oceanic Technol. 30(1):112-126 [doi:10.1175/JTECH-D-12-00043.1].

Frederiksen, M. S., and R. N. Glud. 2006. Oxygen dynamics in the rhizosphere of *Zostera marina*: A two-dimensional planar optode study. Limnol. Oceanogr. 51(2):1072-1083 [doi:10.4319/lo.2006.51.2.1072].

García, H. E., and L. I. Gordon. 1992. Oxygen solubility in seawater: Better fitting equations. Limnol. Oceanogr. 37(6):1307-1312 [doi:10.4319/lo.1992.37.6.1307].

Gruber, N. 2011. Warming up, turning sour, losing breath: ocean biogeochemistry under global change. Phil. Trans. R. Soc. A 369(1943):1980-1996.

Hasumoto, H., T. Imazu, T. Miura, and K. Kogure. 2006. Use of an optical oxygen sensor to measure dissolved oxygen in seawater. J. Oceanogr. 62(1):99-103 [doi:10.1007/s10872-006-0036-8].

Kennan, R. P., and G. L. Pollack. 1990. Pressure dependence of the solubility of nitrogen, argon, krypton, and xenon in water. J. Chem. Phys. 93:2724 [doi:10.1063/1.458911].

Kennish, M. J. (ed.) 1989. Practical handbook of marine science. CRC Press.

Kilimant, I., V. Meyer, and M. Kuhl. 1995. Fiber-optic oxygen microsensors—A new tool in aquatic biology. Limnol. Oceanogr. 40(6):1159-1165 [doi:10.4319/lo.1995.40.6.1159].

Klots, C. E. 1961. Effect of hydrostatic pressure upon the solubility of gases. Limnol. Oceanogr. 6(3):365-366 [doi:10.4319/lo.1961.6.3.0365].

Körtzinger, A., J. Schimanski, U. Send, and D. Wallace. 2004. The ocean takes a deep breath. Science 306(5700):1337-1337 [doi:10.1126/science.1102557].

———, J. Schimanski, and U. Send. 2005. High quality oxygen measurements from profiling floats: A promising new technique. J. Atmos. Oceanic Technol. 22(3):302-308 [doi:10.1175/JTECH1701.1].

Kostov, Y., K. A. Van Houten, P. Harms, R. S. Pilato, and G. Rao.

2000. Unique oxygen analyzer combining a dual emission probe and a low-cost solid-state ratiometric fluorometer. Appl. Spectrosc. 54(6):864-868 [doi:10.1366/0003702001950238].

Lakowicz, J. R. 1999. Principles of fluorescesce spectroscopy, 2nd ed. Academic Press/Plenum Press [doi:10.1007/978-1-4757-3061-6].

Larsen, M., S. M. Borisov, B. Grunwald, I. Klimant, and R. N. Glud. 2011. A simple and inexpensive high resolution color ratiometric planar optode imaging approach: application to oxygen and pH sensing. Limnol. Oceanogr. Methods 9:361-379 [doi:10.4319/lom.2011.9.348].

Li, X. M., and K. Y. Wong. 1992. Luminescent platinum complex in solid films for optical sensing of oxygen. Anal. Chim. Acta 262(1):27-32 [doi:10.1016/0003-2670(92)80004-Q].

Martz, T. R., K. S. Johnson, and S. C. Riser. 2008. Ocean metabolism observed with oxygen sensors on profiling floats in the South Pacific. Limnol. Oceanogr. 53(5):2094-2111 [doi:10.4319/lo.2008.53.5_part_2.2094].

McGinnis, D. F., P. Berg, A. Brand, C. Lorrai, T. J. Edmonds, and A. Wüest. 2008. Measurements of eddy correlation oxygen fluxes in shallow freshwaters: Towards routine applications and analysis. Geophys. Res. Lett. 35(4):L04403 [doi:10.1029/2007GL032747].

McKinley, G. A., M. J. Follows, and J. Marshall. 2000. Interannual variability of the air?sea flux of oxygen in the North Atlantic. Geophys. Res. Lett. 27(18):2933-2936 [doi:10.1029/2000GL011492].

Perry, M. J., B. S. Sackmann, C. C. Eriksen, and C. M. Lee. 2008. Seaglider observations of blooms and subsurface chlorophyll maxima off the Washington coast. Limnol. Oceanogr. 53(5):2169-2179 [doi:10.4319/lo.2008.53.5_part_2.2169].

Revsbech, N. P., L. H. Larsen, J. Gundersen, T. Dalsgaard, O. Ulloa, and B. Thamdrup. 2009. Determination of ultra-low oxygen concentrations in oxygen minimum zones by the STOX sensor. Limnol. Oceanogr. Methods 7:371-381 [doi:10.4319/lom.2009.7.371].

Riser, S. C., and K. S. Johnson. 2008. Net production of oxygen in the subtropical ocean. Nature 451(7176):323-325 [doi:10.1038/nature06441].

Sacksteder, L., J. N. Demas, and B. A. DeGraff, 1993. Design of oxygen sensors based on quenching of luminescent metal complexes: effect of ligand size on heterogeneity. Anal. Chem. 65(23):3480-3483 [doi:10.1021/ac00071a024].

Sinaasappel, M., and C. Ince. 1996. Calibration of Pd-porphyrin phosphorescence for oxygen concentration measurements in vivo. J. Appl. Physiol. 81(5):2297-2303.

Steiner, N., S. Vagle, K. Denman, and C. McNeil. 2007. Oxygen and nitrogen cycling in the northeast Pacific Simulations and observations at Station Papa in 2003/2004. J. Mar. Res. 65(3):441-469 [doi:10.1357/002224007781567658].

Stramma, L., A. Oschlies, and S. Schmidtko. 2012. Mismatch between observed and modeled trends in dissolved upper-ocean oxygen over the last 50 yr. Biogeosciences 9(10):4045-4057 [doi:10.5194/bg-9-4045-2012].

Taylor, C. D. 1978. The effect of pressure upon the solubility of oxygen in water: Implications of the deviation from the Ideal Gas Law upon measurements of fluorescence quenching. Arch. Biochem. Biophys. 191(1):375-384 [doi:10.1016/0003-9861(78)90101-7].

Tengberg, A., J. Hovdenes, H. Andersson, O. Brocandel, R. Diaz, D. Hebert, and A. Stangelmayer. 2006. Evaluation of a lifetimebased optode to measure oxygen in aquatic systems. Limnol. Oceanogr. Methods 4:7-17 [doi:10.4319/lom.2006.4.7].

———, and J. Hovdenes. 2013. Information on long-term stability and accuracy of Aanderaa Oxygen Optodes and Information about multipoint calibration system and sensor option overview. Technical Note issued by Aanderaa Data Instruments AS <http://www.aanderaa.com/media/pdfs/O2-optode-and-calibration.pdf>.

Uchida, H., T. Kawano, I. Kaneko, and M. Fukawawa. 2008. In situ calibration of optode-based oxygen sensors. J. Atmos. Oceanic Technol. 25:2271-2281 [doi:10.1175/2008JTECHO549.1].

———, G. C. Hohnson, and K. E. McTaggert. 2010. CTD oxygen sensor calibration procedures. The GO-SHIP repeat hydrography manual: A collection of expert reports and guidelines, IOCCP Report No. 14, ICPO Publication Series No. 134.

Wikner, J., S. Panigrahi, A. Nydahl, E. Lundberg, U. Båmstedt, and A. Tengberg. 2013. Precise continuous measurements of pelagic respiration in coastal waters with oxygen optodes. Limnol. Oceanogr. Methods 11:1-15 [doi:10.4319/lom.2013.11.1].

*Submitted 30 April 2013*
*Revised 11 December 2013*
*Accepted 28 January 2014*